Polarization-resolved Raman spectroscopy reveals the atomic local ordering in silicon germanium tin epitaxial alloys

Agnieszka Anna Corley-Wiciak,[1,2] Omar Concepción,[3] Marvin Hartwig Zoellner,[1] Gianfranco Sfruncia,[4] Florian Bärwolf,[1] Giuseppe Nicotra,[4] Detlev Grützmacher,[3] Dan Buca,[3] Giovanni Capellini,[1,5] and Davide Spirito[1,*]

[1]*IHP–Leibniz-Institut für Innovative Mikroelektronik, 15236 Frankfurt (Oder), Germany*

[2]*RWTH Aachen University, 52056 Aachen, Germany*

[3]*Peter Grünberg Institute 9 (PGI-9) and JARA-Fundamentals of Future Information Technologies, 52428 Jülich, Germany*

[4]*CNR-IMM, Zona Industriale, Strada VIII 5, 95121 Catania, Italy*

[5]*Dipartimento di Scienze, Università Roma Tre, V.le G. Marconi 446, 00146 Roma, Italy*

(Received 7 May 2024; accepted 13 September 2024; published 4 October 2024)

Ternary SiGeSn alloys have emerged as a promising material system for applications in diverse fields such as photonics, electronics, and thermoelectrics. Its development still requires understanding the alloy properties, where an important role is alleged to be the local arrangement of the Si, Ge, and Sn atoms. Structural properties of SiGeSn epitaxial layers deposited on Ge/Si virtual substrates are investigated here by polarized Raman spectroscopy; in particular, we selected a series of samples with Ge content of ∼83 at.% and variable Si and Sn content. This technique, which provides access not only to the energy but also to the symmetry of the vibrational modes, makes it possible to observe the effect of composition on the local alloy ordering. By studying how the Raman modes change the energy and the relative intensity variation under different polarization configurations, we could isolate the role of alloy configuration as the composition varies. High Sn content appears to promote local ordering, as Sn atoms tend to repel other Sn and Si atoms. Our results are potentially of great interest in elucidating SiGeSn material properties that are still debated in the literature, e.g., the influence of composition on the bandgap directness of the alloy.

DOI: 10.1103/PhysRevMaterials.8.104601

I. INTRODUCTION

Prospective applications in technology-relevant fields, such as optoelectronics, thermoelectric devices, and high-speed transistors, have stimulated intense research on ternary silicon germanium tin (SiGeSn) alloys [1]. In particular, SiGeSn could unleash all its potential in optoelectronic devices [2], such as infrared lasers [3,4], photodetectors [5], and modulators [6]. SiGeSn alloys are macroscopically homogeneous and isotropic, but it has been shown that they are structurally and spatially inhomogeneous at the microscopic level. The crystal structure and atomic arrangement of SiGeSn alloys play a significant role in determining their electronic and optical properties, which are still debated in the literature [7,8]. Several simulation studies have indicated the presence of short-range ordering (SRO) in group IV alloys containing Sn [3,9–12]. It has been observed that the SRO can have a significant impact on the optoelectronic properties of SiGeSn epitaxial alloys; e.g., the band structure is not unambiguously composition dependent, directly affecting the indirect/direct nature of the fundamental bandgap and its value [3,9–12]. Thus, it is difficult to tune precisely the optical properties by adjusting the various "knobs" that can be manipulated during the SiGeSn growth process, such as the composition profile, the thickness, and the lattice strain [4,13–16].

Characterization techniques such as x-ray diffraction (XRD), scanning electron microscopy, and transmission electron microscopy (TEM) provide valuable information on the morphology and lattice parameters of SiGeSn alloys. However, in the case of ternary alloys, many different permutations of composition and strain yield the same lattice parameters [17]. On the other hand, chemically sensitive techniques such as secondary ion mass spectrometry (SIMS) or energy dispersive x-ray spectroscopy, while capable of measuring alloy composition, cannot probe the local arrangement of different atomic species [18]. Other techniques, such as atom probe tomography, require complex instrumentation and are model dependent [19]. Alternatively, polarized Raman spectroscopy has emerged as a powerful tool for crystal structure analysis. This technique provides valuable information about different lattice properties related to its dynamics, crystal order, and composition by analyzing the symmetry of the vibrational modes [20–22]. In binary GeSn alloys, this method has highlighted the relevance of SRO [22]. At the same time, ternary SiGeSn remains more challenging because of the broad parameter space of composition and strain and the richer Raman spectra.

In this paper, we use polarization-resolved Raman spectroscopy to investigate the effect of adding a third species, Si, to the epitaxial GeSn lattice, limiting our scope to a compositional range of interest for optoelectronic applications [1,4,13,14,23,24], i.e., epitaxial layers with approximately

*Contact author: spirito@ihp-microelectronics.com; present address: BCMaterials, Basque Center for Materials, Applications and Nanostructures, UPV/EHU Science Park, 48940 Leioa, Spain; davide.spirito@bcmaterials.net

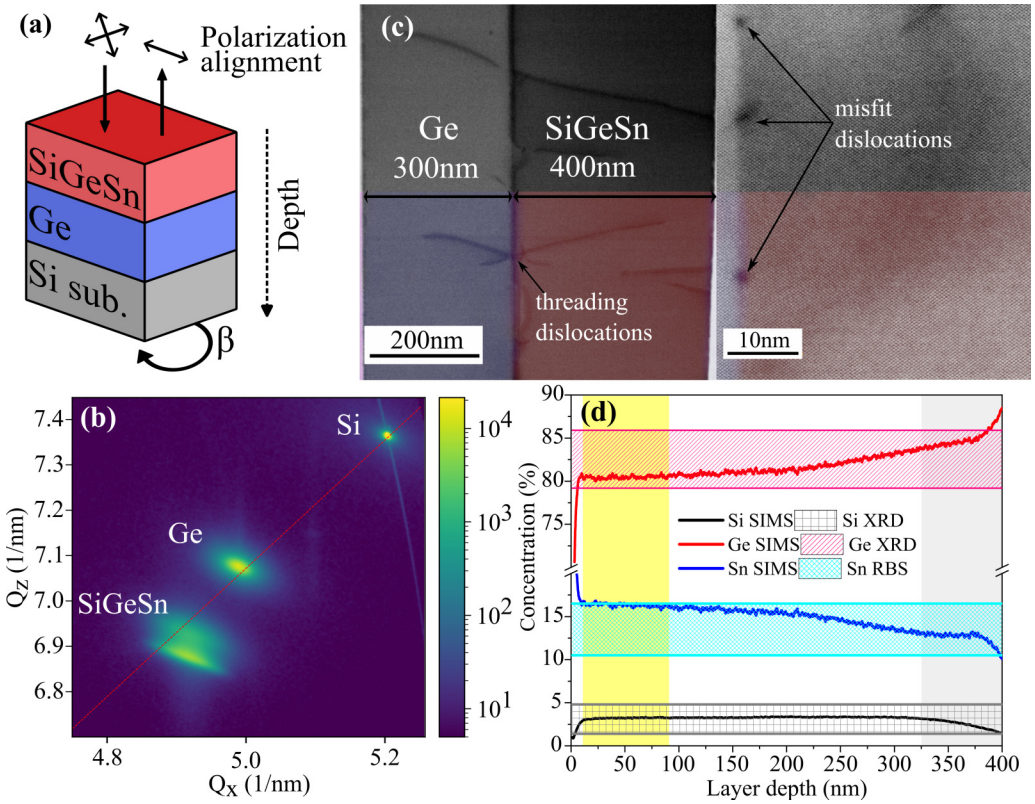

FIG. 1. (a) Scheme of the sample and geometry of the polarized Raman spectroscopy. (b) Reciprocal Space Map of the 224 Bragg reflection for sample Si_2. The dashed-red line indicates a cubic (unstrained) lattice. (c) TEM images of sample Si_2. False colors identify the material (blue, Ge; red, SiGeSn); the right panel is a high-resolution image of the interface. (d) Elemental concentration profile of sample Si_2 for Si, Ge, and Sn obtained by SIMS, XRD, and RBS. The yellow box at depth <80 nm marks the region accessible to Raman spectroscopy.

∼83 at.% Ge content and Si and Sn content ranging from 0 to 16 at.%—including binary alloys silicon-germanium (SiGe) and germanium-tin (GeSn). The separation of different symmetries provided a broader understanding of the alloy vibrational dynamics in response to composition, which was also measured with the help of XRD and SIMS. We can observe the short-range ordering tendency of SiGeSn alloys, particularly Sn atoms' repulsion of other Sn and Si atoms.

II. MATERIALS AND EXPERIMENTAL METHODS

In this study, we investigate SiGeSn layers epitaxially grown on 300-nm Ge/Si(001) [Fig. 1(a)] using an industry-compatible chemical vapor deposition (CVD) reactor. Through controlling the growth parameters, such as the process temperature and the partial pressure of the precursors, samples with different compositions were obtained (see Ref. [15] for details). The Ge content of the layers was kept at approximately 83 at.% in all the samples, while the Sn and Si contents were varied. The atomic concentrations (obtained by SIMS) for the top 80 nm of the SiGeSn layers are presented in Table I, which is the depth probed by the Raman measurement because of the limited penetration of the laser, along with the lattice strain and relaxation values measured by XRD. Rutherford backscattering spectroscopy (RBS) and XRD data for the complete depth of the layers are provided in Table II.

Raman spectroscopy was performed using a Renishaw in Via system, with an excitation energy of 633 nm in backscattering geometry, equipped with a polarizer for the excitation laser and an analyzer at the spectrometer's entrance. The laser is incident along the growth direction [001] (z) [Fig. 1(a)]. The spectra obtained for specific polarization and sample

TABLE I. List of samples with the corresponding atomic composition obtained by SIMS averaging the top 80 nm of the layer, strain and relaxation values obtained by XRD. For SiGeSn, the sample names follow Si concentration.

Sample name	Sn (at.%) SIMS	Ge (at.%) SIMS	Si (at.%) SIMS	Strain XRD (%)	Relaxation XRD (%)
GeSn	14.9	85.1		−0.51	76
Si_2	16.1	81.8	2.1	−0.41	77
Si_4	11.6	84.4	4.0	−0.49	63
Si_8	9.3	83.3	7.5	−0.52	45
Si_11	7.5	81.7	10.8	−0.49	9
SiGe		85.0	15.0	−0.11	97

alignment are related to the crystal directions $x = [100]$, $y = [010]$, $x' = [110]$, and $y' = [1{-}10]$. The polarizer and the analyzer can be oriented parallel or perpendicular to each other. In the following, we fix the analyzer and change the polarizer. The sample can be rotated around the z axis by an azimuth angle β, where $\beta = 0$ is the direction of the analyzer, and the samples are aligned so that $\beta = 0$ corresponds to the $x' = [110]$ direction. Thus, $\beta = 0$ with parallel polarizer and analyzer corresponds to the configuration with Porto notation $z(x'x')\bar{z}$, and $\beta = 45$ deg with perpendicular polarizer is $z(yx)\bar{z}$.

XRD was measured in Bragg diffraction geometry on a Rigaku Smartlab Diffractometer equipped with a rotating Cu Kα source, a Ge 2×220 monochromator, and an x-ray area detector. This allowed for the recording of reciprocal space maps (RSMs) during a single rocking scan. By measuring the 004 and 224 Bragg reflections, we calculated strain and composition in the epitaxial layers. The Sn concentration was fixed for the ternary alloys, considering the SIMS results.

Focused ion beam (FIB) prepared the TEM specimen with utmost care and precision using a Thermofischer Helios 5 UC. After the deposition of carbon protection layers by electron- and ion-beam-induced deposition, the lamella was cut along the [110] direction of the Si substrate. The lamella dimensions are roughly $10\,\mu m \times 5\,\mu m$, with the thinner part being $5\,\mu m \times 4\,\mu m$. We used a probe aberration-corrected JEOL JEM-ARM200F equipped with a cold field emission source with 0.27 eV energy spread, four STEM detectors, a Centurio EDS detector, and a GIF Quantum ER system for electron energy loss spectroscopy (EELS).

Rutherford backscattering spectrometry (RBS) is a powerful technique that allows the extraction of the layers stoichiometry, thickness, and crystalline quality. The spectra were taken at random and channeling alignment using a Tandetron accelerator with 1.4 MeV He^+ ions at a backscattering angle of 170°. RUMP simulation software was used to fit the random spectra, and the degree of crystallinity of the layers was evaluated through the evaluation of the minimum yield, defined as the ratio of the intensity of the channeling and random spectra.

SIMS measurements were performed by an IONTOF V tool equipped with a ToF mass separator. The material was sputtered by Cs^+ ion bombardment with an energy of 500 eV and a sputter area of $300 \times 300\,\mu m^2$. The analysis was performed with single atomic and positively single-charged Bi ions with an energy of 25 keV and an area of $100 \times 100\,\mu m^2$.

III. RESULTS AND DISCUSSION

A. Material characterization and Raman spectra

In order to verify the layer quality and its potential influence on Raman spectra analysis, we used TEM and XRD. Figure 1(b) displays the reciprocal space map of the 224 Bragg reflection of the Si_2 sample, with Si wafer substrate, Ge, and SiGeSn reflections. There are two peaks for SiGeSn at the same in-plane momentum transfer $Q_x \sim 4.9\,nm^{-1}$, belonging to two layers with different stoichiometry, one being pseudomorphic to the other. The two peaks are connected by a line of diffuse scattering, indicating the presence of a transition region between the SiGeSn layers. Additionally, rocking curves of SiGeSn peak are shown in Fig. 7 in the Appendix for all the SiGeSn samples. Figure 1(c) shows TEM images of the same sample to analyze the dislocation caused during the relaxation process. We can observe a dense misfit dislocation network at the Ge/SiGeSn interface because of the plastic relaxation process and few threading dislocations propagating from the Ge buffer layer towards the sample surface through the Ge/SiGeSn heterointerface, where some of the threading dislocations are observed to bend, possibly connecting to misfit dislocations and fostering relaxation of the SiGeSn layer, similar to what has been observed in the Ge/SiGe system [25].

The other vital factor in understanding the local ordering of the alloys is the content and its homogeneity across the layers. Figure 1(d) depicts a profile of elemental composition obtained by SIMS on the Si_2 sample, providing a comparative analysis with the data obtained through XRD and RBS measurements (see Table II in the Appendix). XRD and RBS analysis showed two layers in this case, with different content–maximum and minimum of the boxes in Fig. 1(c). Notably, a distinct pattern emerges across all samples, revealing a gradual increase in Si content within the initial 100 nm of growth [a grey area in Fig. 1(c), at a depth larger than 330 nm]. For samples featuring higher Sn content (Si_4, Si_2), a discernible gradual transition into a distinct second layer of even higher Sn concentration is observed [Fig. 1(a)], while lower Sn content samples (Si_8, Si_11) exhibit a more gradual transition (Fig. 6 in Appendix). The observed behavior aligns with the previous study on GeSn and SiGeSn epitaxy [22,26], which found an enhancement in (Si)Sn concentration above the critical thickness for plastic strain relaxation [7,27]. The different degrees of plastic relaxation between the samples is evidenced by a change in rocking curve width, as demonstrated in Fig. 7 in the Appendix. However, the observed variations in layer composition do not significantly impact the Raman spectra analysis, as the depth probed by Raman is limited below ~80 nm by the layer absorption, where the atomic concentration remains constant.

Figure 2 displays Raman spectra in four polarization configurations for different samples: Ge, SiGe, GeSn, and SiGeSn-Si_2 (the spectra of the other samples can be found in Fig. 8 in the Appendix). The first-order Raman spectrum of group-IV cubic semiconductors with diamond structure (point group O_h, m3m) has a single peak. In backscattering geometry, when the incidence is along the ⟨100⟩ direction, this peak corresponds to longitudinal optical (LO) phonons belonging to the T_{2g} representation and is only visible in the polarization configurations $z(yx)\bar{z}$ and $z(x'x')\bar{z}$. Other potentially active representations for the O_h group are A_{1g}, found in the configurations $z(x'x')\bar{z}$ and $z(xx)\bar{z}$, and E_g, which is active in all configurations except the $z(yx)\bar{z}$ [22]. The polarization configuration thus affects the intensity of the peaks according to the associated symmetry of the mode. The spectra in Fig. 2 were measured with the same acquisition conditions except for the polarization. The left column of the figure shows how most of the peaks follow these selection rules for the T_{2g} (LO) symmetry, in particular, the main peak around $300\,cm^{-1}$ associated with Ge-Ge pairs vibrations. When it is suppressed, e.g., in the configuration $z(xx)\bar{z}$, modes with different symmetry dominate the spectra. Each spectrum in the right

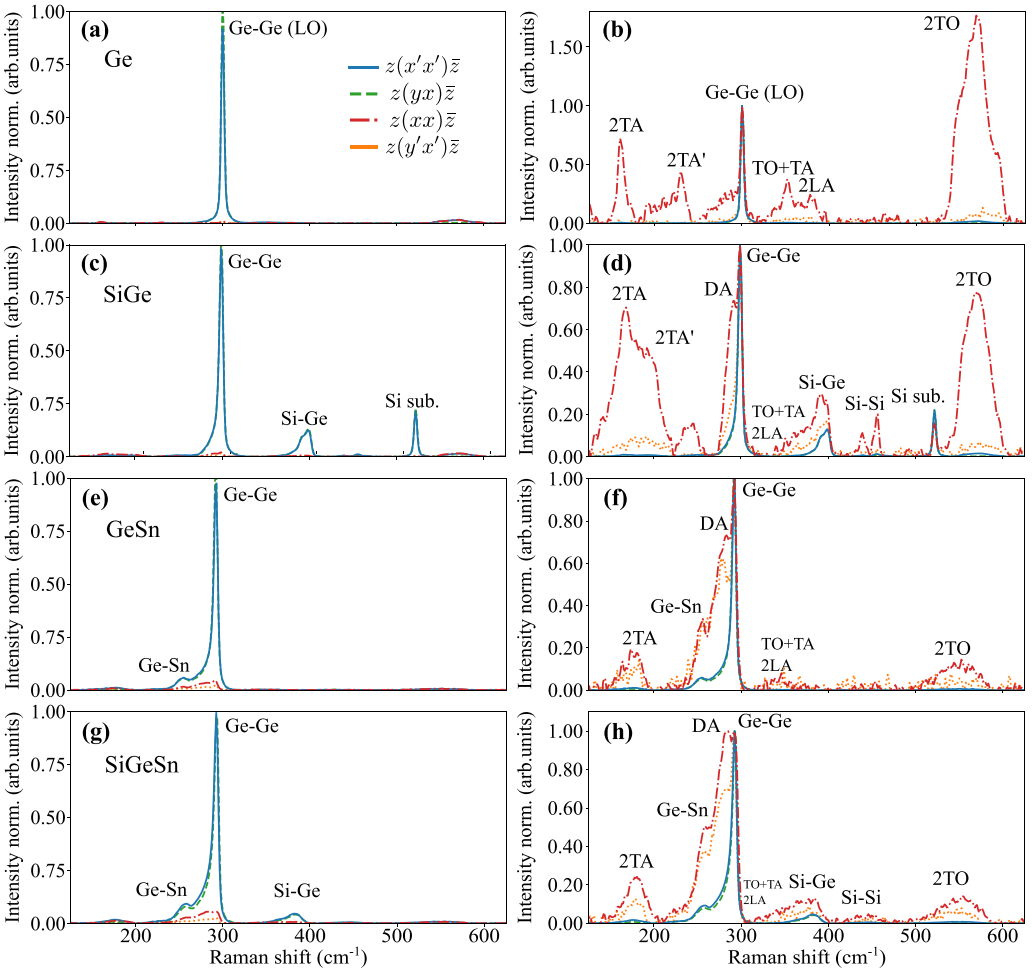

FIG. 2. Raman spectra in four different polarization configurations of (a), (b) Ge, (c), (d) SiGe, (e), (f) GeSn, and (g), (h) SiGeSn (Si_2) samples. (Left panels) Spectra are normalized to Ge-Ge peak in $z(yx)\bar{z}$ configuraration. (Right panels) Each spectrum is normalized to Ge-Ge peak maximum.

panels was normalized to the Ge-Ge peak to highlight this behavior. This highlights the much richer landscape of peaks; for example, the overtones 2TO and 2TA (second-order transverse optical and acoustic modes, respectively) are evident after this normalization since their intensity is comparable to the weak Ge-Ge peak when it is suppressed.

In the Ge sample [Figs. 2(a) and 2(b)], the spectra are dominated by LO phonon at $\sim$300 cm^{-1} in $z(yx)\bar{z}$ and $z(x'x')\bar{z}$ configurations. These spectra serve as reference to distinguish secondary modes and overtones, which can be clearly observed in $z(xx)\bar{z}$ configuration, and in $z(x'x')\bar{z}$. In those configurations, there are two 2TA at $\sim$160 cm^{-1} and $\sim$230 cm^{-1}. In $z(yx)\bar{z}$ we can observe instead one peak at $\sim$190 cm^{-1}. Combination modes are also observed, such as TO+TA at 355 cm^{-1}, the second-order longitudinal acoustic (2LA) at 380 cm^{-1}, and between 540 cm^{-1} and 600 cm^{-1}, the group of three modes overlapping 2TO [25,28]. When considering the SiGe alloy, in addition to the primary and secondary modes assigned to Ge-Ge pairs, a discernible double Si-Ge mode emerges at $\sim$400 cm^{-1}, and two Si-Si modes at $\sim$430 cm^{-1} and $\sim$450 cm^{-1} [29–31]. In addition, a shoulder of Ge-Ge peak can be observed at $\sim$290 cm^{-1}, especially in the $z(xx)\bar{z}$ configuration assigned to a disorder-induced activation of phonon density of states (DA). In the case of the secondary 2TA, the distance between the two component modes is reduced, and the 2TO component modes are less distinguishable than in Ge. Moving on to the GeSn alloy with 15 at.% Sn, a distinct Ge-Sn peak emerges at around 260 cm^{-1}, accompanied by a shoulder of similar intensity as observed in the SiGe spectra (disorder-activated mode, DA) [22,28]. The neighboring secondary Ge peaks overlap so we can observe a single band of 2TA peaks with a maximum at $\sim$175 cm^{-1}, a very weak TO+TA together with 2LA, and a broad 2TO mode. The final panel shows the SiGeSn spectra of sample Si_11. A combination of modes observed for SiGe and GeSn alloys is evident [25,29,32,33]. Si-Ge peak tends to overlap with secondary Ge peaks, and there is no distinguishable double peak as in the case of SiGe. Moreover, the Si-Si is a broad single band between 400 cm^{-1} and 500 cm^{-1}. The 2TA mode, similar to GeSn, appears as one peak. We notice that no features that can be attributed to the Si-Sn mode are observed.

To summarize, Raman spectra in four polarization configurations for Ge, SiGe, GeSn, and SiGeSn samples revealed the dominance of the Ge-Ge peak in LO symmetry and the emergence of secondary modes in non-LO

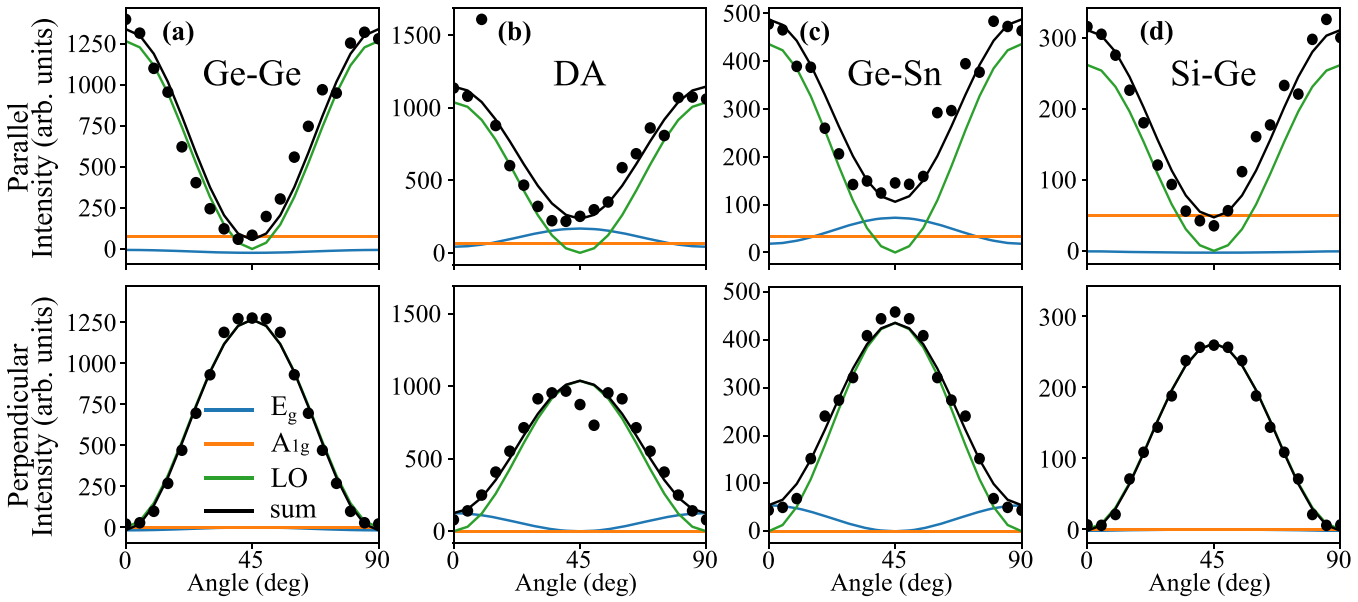

FIG. 3. Angular dependence of (a) Ge-Ge, (b) DA, (c) Ge-Sn, (d) Si-Ge peaks intensity for the sample Si_2, analyzed with a combination of different representations (E_g, A_{1g}, LO).

configurations. The polarization configurations significantly affected peak intensities, highlighting the influence of vibrational mode symmetries. The Raman spectra revealed complex vibrational dynamics influenced by the ternary composition, with significant contributions from LO and non-LO symmetries, which we aim to study not only qualitatively, but also quantitatively to improve the understanding of the local ordering of SiGeSn alloys.

B. Polarization dependence

A more quantitative understanding of the vibrational mode symmetry can be obtained scanning over the relative alignment of sample and polarization direction, for each vibrational mode. While the spectra in Fig. 2 considers only four selected alignments, Fig. 3 reports the analysis of the intensity variation as a function of the azimuth angle and for the two polarization alignments, for sample Si_2. The spectra have been collected in parallel (upper panels) and perpendicular (lower panels) geometry of polarizer and analyzer, at 5 deg step between 0 deg ([110] crystal direction) and 90 deg ([100] direction). The details of the peaks fitting are shown in Fig. 9 in the Appendix. The integrated peak area has been used for the analysis. The peak intensities as a function of azimuth angle were fitted by a sum of angular dependence for the T_{2g}(LO), A_{1g}, and E_g representations [14] to estimate of their relative weight.

While the angular dependence of the Ge-Ge modes is fully captured by the T_{2g}(LO) mode, the DA mode is a composite of all active representations, as previously identified in GeSn alloys [22]. However, the ternary composition of SiGeSn introduces additional complexity. Notably, the Ge-Sn and Si-Ge cannot be fully reproduced by the T_{2g}(LO) symmetry alone, unlike the GeSn case. This observation is particularly evident in the intensity values at 45 deg in parallel polarization, a feature not observed in GeSn systems.

The relative weight of LO and non-LO ($A_{1g} + E_g$) components provides detailed insights into the influence of content on these distinct vibrational modes, since LO symmetry can be associated with pair vibrations in the cubic crystal. At the same time, non-LO is instead a sign of disorder-activated modes. For this sample Si_2, non-LO is negligible for the main Ge-Ge peak, but becomes larger than 10% for the other peaks. This relative weight can be used as guiding parameter to compare the alloy across the various composition and the role of local ordering.

C. Dependence on Si content

The effect of composition is often observed in the spectra as a difference in relative intensity and in the peak position of peaks associated with different atom pairs. Here, we additionally apply the polarization analysis reported above to the set of ternary SiGeSn and binary (GeSn and SiGe) alloy samples. Comparison of LO and non-LO modes is expected to give hints of the local ordering in the alloy.

Figure 4 shows the relative weight of the individual components LO, A_{1g}, and E_g as a function of Si content for each peak. For all the peaks, the dominant contribution is LO (>80%), and the second is the A_{1g} component, which is around 5–20%. These weights are, however, different among the peaks.

The main Ge-Ge peak has a negligible non-LO component (<10%) for all the samples. In the other peaks, the non-LO components are more relevant (10–20%), particularly for the ternary SiGeSn case. This is supported by the analysis of peak energy (Fig. 10 in the Appendix), where we find that DA has a clear energy difference between LO and non-LO symmetry, similar to the result in binary GeSn, because the DA-LO and DA-non-LO are two different modes [22]. Such energy splitting can also be observed for Si-Ge and Ge-Sn peaks. The weight and spitting of non-LO composition on

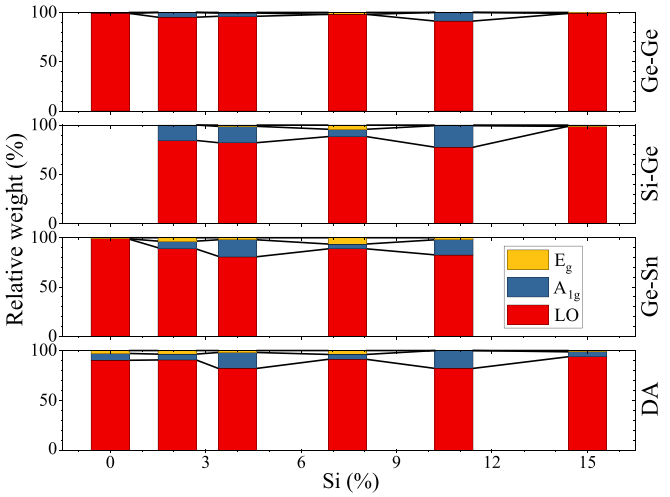

FIG. 4. Weight of different components on each peak for all the samples as a function of Si content.

Si-Ge and Ge-Sn peaks in SiGeSn, similar to the DA case, indicates that they cannot be described as first-order Raman scattering pairs of atoms in a diamond lattice, differently from binary GeSn [21].

This deviation from pure T_{2g}(LO) mode behavior suggests that the vibrational dynamics in SiGeSn alloys involve a more intricate interplay of modes, reflective of the distinctive elemental composition within the ternary system.

We thus focus, in Fig. 5, on the spectral weight of each peak, i.e., the ratios of the DA, Ge-Sn, Ge-Ge, and Si-Ge intensity to the total intensity, for LO symmetry and non-LO symmetry, and for all the samples. Since the LO is associated with pair vibrations, it can be expected to depend on composition (e.g., the more the Si, the stronger the Si-Ge peak). In comparison, the non-LO can hint at local ordering.

As expected because of the composition of ∼83 at.% Ge, the Ge-Ge peak dominates in the LO case and is weak in non-LO. In LO, the Si-Ge peak increases as the Si content increases, as expected. For the non-LO, the Si-Ge is significantly stronger for the ternary SiGeSn than for the binary SiGe and GeSn, with a weak dependence on Si content. A similar trend is observed for the Ge-Sn, but surprisingly, the Ge-Sn intensity follows the Sn content in non-LO symmetry and simultaneously remains constant in LO. This suggests that the alloy disorder in ternary alloys plays a relevant role in these atom pairs.

We then look at the DA feature, a sensitive probe of the local arrangement. As mentioned, the DA is the convolution of two modes with different energies. One is active in LO symmetry with energy close to the main Ge-Ge vibration. It arises from the Ge-Ge pairs whose vibration is affected by the nearby environment, presenting short-range ordering with Sn clustering [22]. The second has lower energy and is strong in non-LO configuration, and is associated with alloy disorder. The DA is the strongest peak in the non-LO case, especially for the binary alloys, and in SiGeSn its intensity slightly decreases with higher Si content, which indicates that alloy disorder is weakly correlated with the amount of heavy Sn atoms. In the LO case, the DA is almost comparable with main Ge-Ge for GeSn and SiGeSn but is much weaker

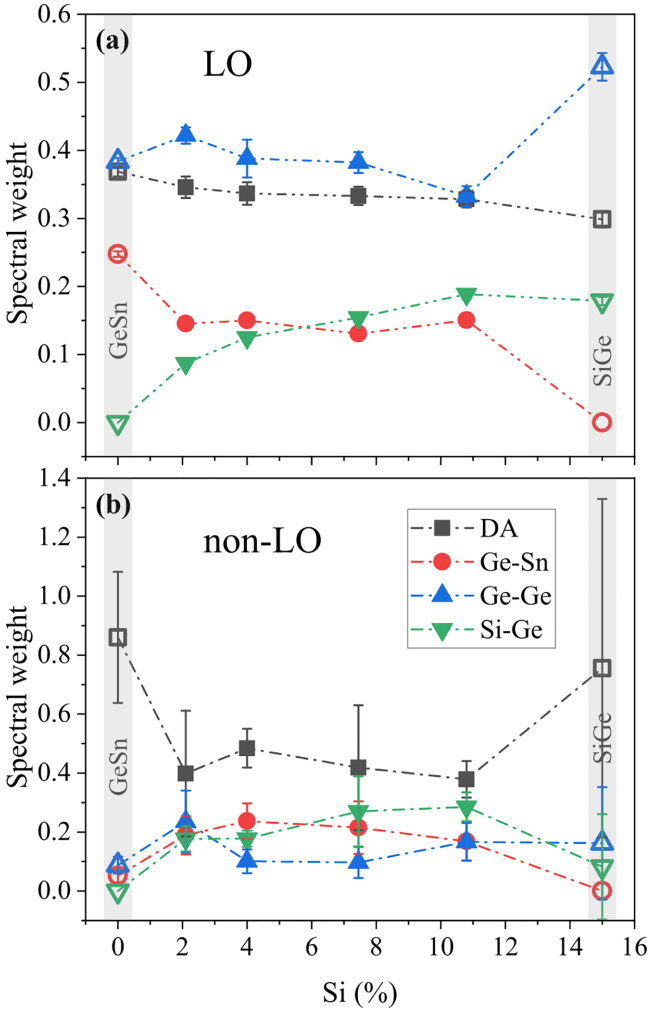

FIG. 5. Dependence of the Si content on fraction of DA, Ge-Sn, Ge-Ge, and Si-Ge peaks intensity for SiGeSn samples (full symbols) with varying content, SiGe (15%), and GeSn (0%) (empty symbols) in (a) LO, (b) non-LO symmetry ($A_{1g} + E_g$).

than Ge-Ge for SiGe. This suggests that in SiGe, which is a completely miscible, random alloy [30], DA is mainly associated with genuine disorder-assisted vibrations (the feature is also labeled "quasi-amorphous" in the literature). The local environment of Ge-Ge pairs is less distorted in SiGe than in GeSn and SiGeSn, and the averaged alloy affects all the pairs.

The short-range order of SiGeSn alloys has been studied previously by theoretical simulations [9] and extended x-ray absorption fine structure (EXAFS) experiment [34], which indicate the short-range order in SiGeSn alloy, where, similar to other group IV alloys with Sn [10,35], the Sn atoms repulse each other. Moreover, the Si and Sn atoms tend to show mutual repulsion. Theoretical studies [3,9] predicted two types of short-range order in SiGeSn, one of which, the enhanced-SRO (E-SRO), has a lower coordination number for Ge (i.e., less Ge-Ge pairs), with strong repulsion of Sn-Sn and Si-Sn nearest neighbors, and was shown to be energetically favorable. The Ge atoms make more pairs with Si and Sn than expected from composition, which would explain the higher level of lattice distortion around Ge atoms since they are

simultaneously affected as atoms of different sizes. In Raman spectra, this results in a relevant DA-LO peak. At the same time, the alloy disorder is weakly affected by the compositions as soon as three species are present, as seen from the rather constant composition dependence of non-LO components.

Our findings align with theoretical simulations, indicating short-range order in SiGeSn alloys, characterized by repulsive interactions between Sn atoms and mutual repulsion between Si and Sn atoms.

IV. CONCLUSIONS

The comprehensive investigation of ternary SiGeSn epitaxial layers on a Ge substrate presented in this work provided insights into their vibrational and structural properties. The study revealed a nuanced dependence of peak intensities on content variation within the SiGeSn alloy system. The angular study of the intensities of the DA, Ge-Sn, Ge-Ge, and Si-Ge peaks allows the analysis of the symmetries of individual spectral components. It reveals their mixed nature associated with lattice deformation. The separation of different symmetries provided a broader understanding of the vibrational dynamics of the alloy as a function of composition. The difference between binary GeSn and SiGe and ternary SiGeSn alloys for the Raman peaks associated with different atom pairs indicated a specific short-range ordering of SiGeSn, which resulted in a strong signal from Ge-Ge pairs in a distorted environment. We can observe higher intensities of Ge-Sn and Si-Ge vibrations for disorder-associated symmetries. These results are compatible with the picture that Sn atoms tend to repel other Sn and Si atoms. Our results contribute to a broader understanding of SiGeSn alloy systems by providing a detailed perspective on their vibrational and structural intricacies.

APPENDIX

The atomic concentration and thickness of the layers were determined through Rutherford backscattering spectroscopy (RBS) and secondary ion mass spectrometry (SIMS). The obtained results were further validated and refined through meticulous x-ray diffraction (XRD) analysis. This multifaceted characterization strategy ensures the reliability of measurements of the compositional structure of the SiGeSn layers.

The layer quality can be indicated by width of XRD rocking curve. The increasing width of the rocking curve in $\Delta\omega$ corresponds to a greater density of structural defects and a degradation of crystal quality. Figure 7 shows the comparison of rocking curve around SiGeSn, GeSn, and SiGe peaks of analyzed SiGeSn, GeSn, and SiGe samples respectively. The results show small variations of crystalline quality. Sample Si_11 exhibits a narrower peak; because of its composition, this sample is pseudomorphic to the Ge substrate, and consequently is free of dislocations.

The Raman spectra obtained for samples Si_8, Si_4, and Si_11 are shown in Fig. 8. With increasing the Sn content, we observe a decrease in relative intensities of secondary Ge peaks, such as 2TA and 2TO.

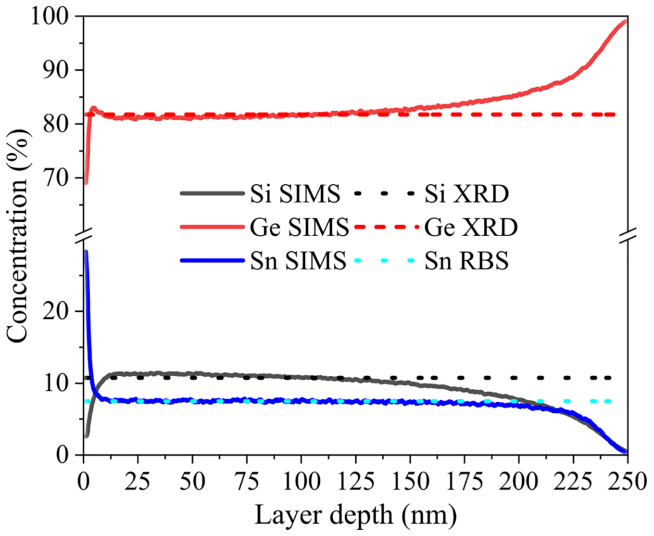

FIG. 6. Concentration profile of Si, Ge, and Sn obtained by SIMS, XRD, and RBS of sample Si_11.

To replicate the Ge-Ge mode asymmetry in the quantitative analysis of the peaks, we used exponentially modified Gaussian (EMG) line shape. The Ge-Sn, DA, and Si-Ge peaks were fitted using Gaussian functions. The fitting of the group around the main peak (Ge-Ge, DA, and Ge-Sn peaks) is shown in Figs. 9(a) and 9(b), while the Si-Ge is shown in Figs. 9(c) and 9(d).

Figure 10 displays the change of peaks' position of SiGeSn as a function of Si content for different symmetries. As the Si content increases, all spectral features tend to move toward higher energies. The Ge-Ge and Ge-Sn peak positions are independent of the symmetry within the error in the whole content range. In the case of Si-Ge and DA, a significant difference in the peak position appears for the LO and non-LO.

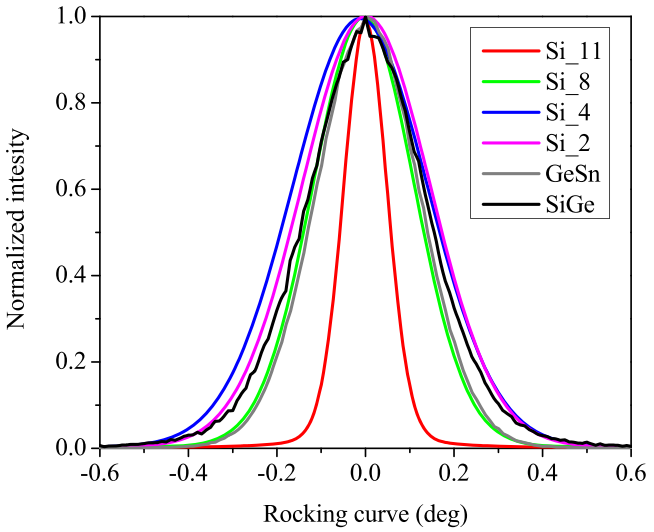

FIG. 7. Normalized intensity XRD rocking curve I($\Delta\omega$) of series of SiGeSn, GeSn, and GeSn samples.

TABLE II. List of SiGeSn samples with thickness and content obtained by different methods. Components are indicated in order of growth. The XRD values are obtained with an iterative procedure in comparison with SIMS data.

Sample	SiGeSn thickness SIMS (nm)	Sn (at.%) XRD	Sn (at.%) RBS	Sn (at.%) SIMS	Si (at.%) XRD	Si (at.%) SIMS	Ge (at.%) XRD	Ge (at.%) SIMS
Si_2	400	13/15.8	10.5/13.5/16.5	12.4–16.8	2.6/4.1	1.7–3	84.4/80.1	86.5–80.7
Si_4	225	10.6/11.8	10/11.8	9.5–12	3.9/5.3	3.3–5	85.5/82.9	87.2–85.9
Si_8	190	9.4	9/10	7.5–9.8	7.7	3.7–7.4	82.9	88.6–82.8
Si_11	240	7.6	7.5	6–7.6	11.3	5.8–11.6	81.1	88–81.5

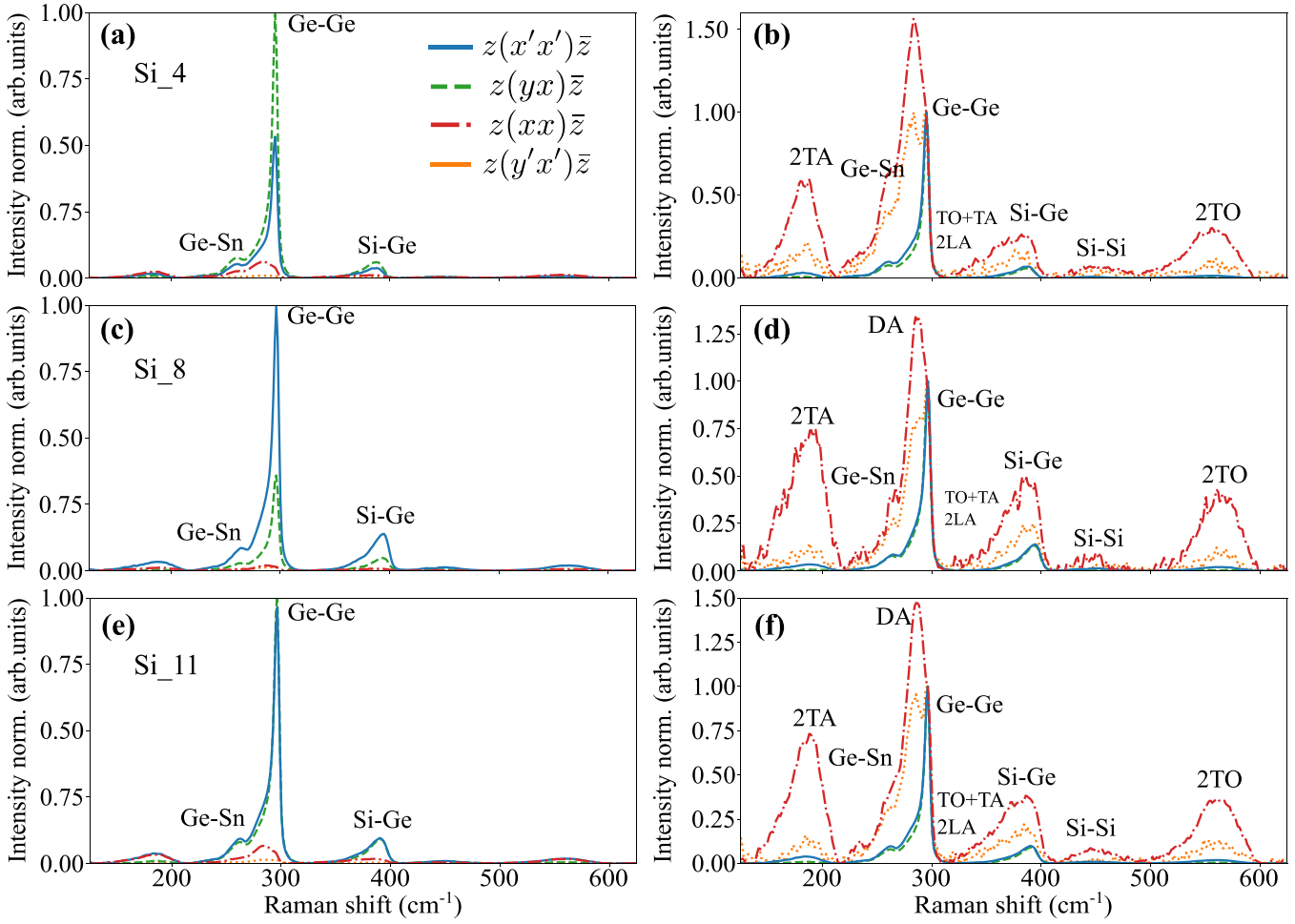

FIG. 8. Raman spectra in four different polarization configurations of the samples (a), (b) Si_4, (c), (d) Si_8, and (e), (f) Si_11. (Left panels) Spectra are normalized to Ge-Ge peak in $z(yx)z$ configuration. (Right panels) Each spectrum is normalized to Ge-Ge peak maximum.

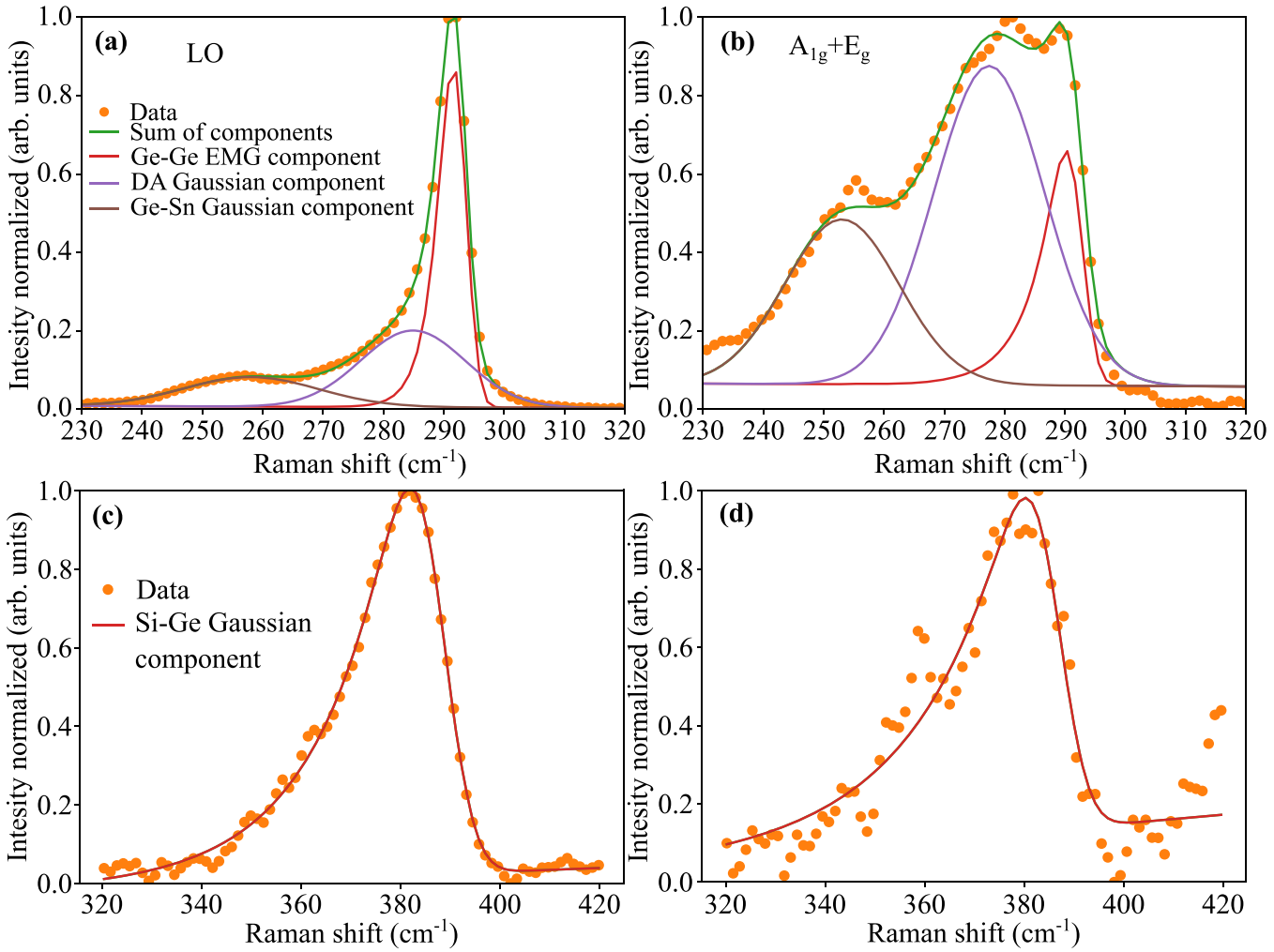

FIG. 9. Fitting of Ge-Ge, DA, and Ge-Sn peaks (a), (b) and Si-Ge peak (c), (d) in polarized configurations: $z(xx)\bar{z}$ (left panels) and $z(x'x')\bar{z}$ (right panels) of sample Si_2.

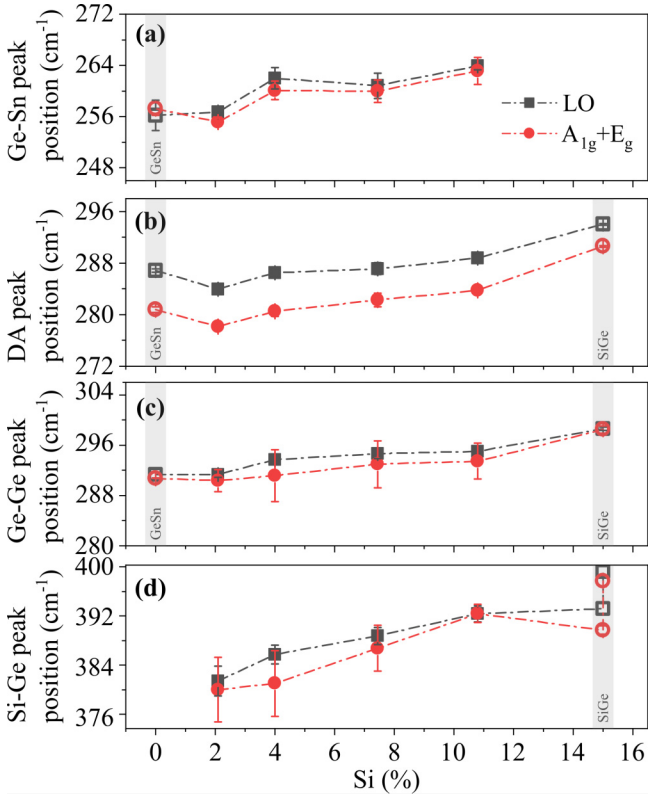

FIG. 10. Peak position of (a) Ge-Ge, (b) DA, (c) Ge-Sn, (d) Si-Ge peaks as a function of Si content in different symmetry, obtained from polarization configuration $z(xx)\bar{z}$ (LO) and $z(y'x')\bar{z}$ (non-LO).

[1] N. von den Driesch, Advanced GeSn/SiGeSn group IV heterostructure lasers, Adv. Sci. **5**, 1700955 (2018).

[2] O. Moutanabbir, Monolithic infrared silicon photonics: The rise of (Si)GeSn semiconductors, Appl. Phys. Lett. **118**, 110502 (2021).

[3] X. Jin, S. Chen, C. Lemkan, and T. Li, Role of local atomic short-range order distribution in alloys: Why it matters in Si-Ge-Sn alloys, Phys. Rev. Mater. **7**, L111601 (2023).

[4] W. Du, Investigation of optical transitions in a SiGeSn/GeSn/SiGeSn single quantum well structure, J. Appl. Phys. **122**, 123102 (2017).

[5] I. A. Fischer, Growth and characterization of SiGeSn quantum well photodiodes, Opt. Express **23**, 25048 (2015).

[6] Z. Chen, Z. Ikonic, D. Indjin, and R. W. Kelsall, Design considerations of intra-step SiGeSn/GeSn quantum well electroabsorption modulators, J. Appl. Phys. **130**, 153103 (2021).

[7] S. Assali, A. Dijkstra, A. Attiaoui, É. Bouthillier, J. E. M. Haverkort, and O. Moutanabbir, Midinfrared emission and absorption in strained and relaxed direct-band-gap $Ge_{1-x}Sn_x$ semiconductors, Phys. Rev. Appl. **15**, 024031 (2021).

[8] T. Wendav, Compositional dependence of the band-gap of $Ge_{1-x-y}Si_xSn_y$ alloys, Appl. Phys. Lett. **108**, 242104 (2016).

[9] X. Jin, S. Chen, and T. Li, Coexistence of two types of short-range order in Si–Ge–Sn medium-entropy alloys, Commun Mater **3**, 66 (2022).

[10] B. Cao, S. Chen, X. Jin, J. Liu, and T. Li, Short-range order in GeSn alloy, ACS Appl. Mater. Interfaces **12**, 57245 (2020).

[11] S. Mukherjee, N. Kodali, D. Isheim, S. Wirths, J. M. Hartmann, D. Buca, D. N. Seidman, and O. Moutanabbir, Short-range atomic ordering in nonequilibrium silicon-germanium-tin semiconductors, Phys. Rev. B **95**, 161402(R) (2017).

[12] S. Chen, X. Jin, W. Zhao, and T. Li, Intricate short-range order in GeSn alloys revealed by atomistic simulations with highly accurate and efficient machine-learning potentials, Phys. Rev. Mater. **8**, 043805 (2024).

[13] V. R. D'Costa, Y.-Y. Fang, J. Tolle, J. Kouvetakis, and J. Menéndez, Ternary GeSiSn alloys: New opportunities for strain and band gap engineering using group-IV semiconductors, Thin. Solid. Films **518**, 2531 (2010).

[14] G. Abernathy, S. Ojo, A. Said, J. M. Grant, Y. Zhou, H. Stanchu, W. Du, B. Li, and S.-Q. Yu, Study of all-group-IV SiGeSn mid-IR lasers with dual wavelength emission, Sci. Rep. **13**, 18515 (2023).

[15] D. Grützmacher, O. Concepción, Q.-T. Zhao, and D. Buca, Si–Ge–Sn alloys grown by chemical vapour deposition: A versatile material for photonics, electronics, and thermoelectrics, Appl. Phys. A **129**, 235 (2023).

[16] J. Xie, A. V. G. Chizmeshya, J. Tolle, V. R. D'Costa, J. Menendez, and J. Kouvetakis, Synthesis, stability range, and fundamental properties of Si−Ge−Sn semiconductors grown directly on Si(100) and Ge(100) platforms, Chem. Mater. **22**, 3779 (2010).

[17] R. Khazaka, E. Nolot, J. Aubin, and J.-M. Hartmann, Growth and characterization of SiGeSn pseudomorphic layers on

200 mm Ge virtual substrates, Semicond. Sci. Technol. **33**, 124011 (2018).

[18] W. Dou, Investigation of GeSn strain relaxation and spontaneous composition gradient for low-defect and high-Sn alloy growth, Sci. Rep. **8**, 5640 (2018).

[19] B. Gault, A. Chiaramonti, O. Cojocaru-Mirédin, P. Stender, R. Dubosq, C. Freysoldt, S. K. Makineni, T. Li, M. Moody, and J. M. Cairney, Atom probe tomography, Nat. Rev. Methods Primers **1**, 51 (2021).

[20] A. Cui, X. Cao, Y. Ye, K. Jiang, L. Zhu, M. Jiang, G. Rao, Y. Li, Z. Hu, and J. Chu, Phase transitions and phonon thermodynamics in giant piezoelectric Mn-doped $K_{0.5}Na_{0.5}NbO_3$-$LiBiO_3$ crystals studied by Raman spectroscopy, Phys. Rev. B **102**, 214102 (2020).

[21] R. S. Alencar, R. Longuinhos, C. Rabelo, H. Miranda, B. C. Viana, A. G. Souza Filho, L. G. Cançado, A. Jorio, and J. Ribeiro-Soares, Raman spectroscopy polarization dependence analysis in two-dimensional gallium sulfide, Phys. Rev. B **102**, 165307 (2020).

[22] A. A. Corley-Wiciak, S. Chen, O. Concepción, M. H. Zoellner, D. Grützmacher, D. Buca, T. Li, G. Capellini, and D. Spirito, Local alloy order in a $Ge_{1-x}Sn_x$/Ge epitaxial layer, Phys. Rev. Appl. **20**, 024021 (2023).

[23] B. Marzban, Strain engineered electrically pumped SiGeSn microring lasers on Si, ACS Photonics **10**, 217 (2023).

[24] N. von den Driesch, SiGeSn ternaries for efficient group IV heterostructure light emitters, Small **13**, 1603321 (2017).

[25] V. R. D'Costa, J. Tolle, C. D. Poweleit, J. Kouvetakis, and J. Menéndez, Compositional dependence of Raman frequencies in ternary $Ge_{1-x-y}Si_xSn_y$ alloys, Phys. Rev. B **76**, 035211 (2007).

[26] J. Margetis, Fundamentals of $Ge_{1-x}Sn_x$ and $Si_yGe_{1-x-y}Sn_x$ RPCVD epitaxy, Mater. Sci. Semicond. Process. **70**, 38 (2017).

[27] H. V. Stanchu, A. V. Kuchuk, Y. I. Mazur, K. Pandey, F. M. de Oliveira, M. Benamara, M. D. Teodoro, S.-Q. Yu, and G. J. Salamo, Quantitative correlation study of dislocation generation, strain relief, and Sn outdiffusion in thermally annealed GeSn epilayers, Cryst. Growth Des. **21**, 1666 (2021).

[28] É. Bouthillier, S. Assali, J. Nicolas, and O. Moutanabbir, Decoupling the effects of composition and strain on the vibrational modes of GeSn, Semicond. Sci. Technol. **35**, 095006 (2020).

[29] S. Nakashima, T. Mitani, M. Ninomiya, and K. Matsumoto, Raman investigation of strain in Si/SiGe heterostructures: Precise determination of the strain-shift coefficient of Si bands, J. Appl. Phys. **99**, 053512 (2006).

[30] O. Pagès, J. Souhabi, V. J. B. Torres, A. V. Postnikov, and K. C. Rustagi, Re-examination of the SiGe Raman spectra: Percolation/one-dimensional-cluster scheme and *ab initio* calculations, Phys. Rev. B **86**, 045201 (2012).

[31] A. Picco, E. Bonera, E. Grilli, M. Guzzi, M. Giarola, G. Mariotto, D. Chrastina, and G. Isella, Raman efficiency in SiGe alloys, Phys. Rev. B **82**, 115317 (2010).

[32] J. Schlipf, Raman shifts in MBE-grown $Si_xGe_{1-x-y}Sn_y$ alloys with large Si content, J Raman Spectroscopy **52**, 1167 (2021).

[33] A. B. Talochkin, V. A. Timofeev, A. K. Gutakovskii, and V. I. Mashanov, Sn–induced decomposition of SiGeSn alloys grown on Si by molecular-beam epitaxy, J. Cryst. Growth **478**, 205 (2017).

[34] Y. Shimura, T. Asano, T. Yamaha, M. Fukuda, W. Takeuchi, O. Nakatsuka, and S. Zaima, EXAFS study of local structure contributing to Sn stability in $Si_yGe_{1-y-z}Sn_z$, Mater. Sci. Semicond. Process. **70**, 133 (2017).

[35] X. Jin, S. Chen, and T. Li, Short-range order in SiSn alloy enriched by second-nearest-neighbor repulsion, Phys. Rev. Mater. **5**, 104606 (2021).